SUPPLEMENTARY MATERIAL
Do Different Tracking Tasks Require Different Appearance Models?

A Datasets and Evaluation Metrics

The table below summarizes the datasets (all publicly available) and evaluation metrics used in this work. In general, to compare with existing task-specific methods, we use the most popular benchmark for each task and report the standard metrics.

For association-type tasks (MOT, MOTS and PoseTrack), we first report the MOTA metric since it highly-correlates with human's perception in measuring tracking accuracy [3]. However, the MOTA metric disproportionately overweights good detection accuracy [28, 8]. Since most multi-object trackers (included UniTrack) adopt off-the-shelf detectors, it is desirable to also adopt detection-independent measures of performance. For this reason, we also report identity based metrics such as IDF-1 and ID-switch. We also adopt the recently-introduced higher-order HOTA [28], to replace MOTA and to represent the overall tracking accuracy when comparing self-supervised methods.

For pose tracking, results are averaged for IDF-1 and MOTA, and summed for ID-switch, over 15 key points. In the main text, we only report results for the first five tasks from the table below. For the rest tasks (PoseProp and VIS) we provide additional results in Appendix E. We also provide SOT results on many more recent large-scale datasets in Appendix F.

Task	SOT	VOS	MOT	MOTS	PoseTrack	PoseProp	VIS
Dataset	OTB [50]	DAVIS 2017 [32]	MOT 16 [29]	MOTS [43]	PoseTrack 2107 [2]	JHMDB [18]	YoutubeVIS [52]
Metrics	AUC	$\mathcal{J}$-mean	IDF1 MOTA	IDF1 sMOTA	IDF1 MOTA ID-switch (IDs)	PCK	mAP

A single run of the evaluation on five tasks takes about 2 hours in a Titan Xp GPU.

B *Propagation*

B.1 Box Propagation

In order to propagate bounding boxes, we adopt two methods relying on fully-convolutional Siamese [5, 40, 45, 23] networks. Given a target image patch I_x that contains the object of interest, and a search image patch I_z (typically a larger search area in the next frame), the appearance model ϕ processes both patches and outputs their feature maps $x = \phi(I_x)$ and $z = \phi(I_z)$.

Cross-correlation (XCorr) head. As in SiamFC [5], we simply cross-correlate the two feature maps, yielding the response map

$$g(x, z) = x \star z \tag{1}$$

Eq. 1 is equivalent to performing an exhaustive search of the pattern x over the search region z. The location of the target object can be determined by finding the maximum value of response map.

Discriminative Correlation Filter (DCF) head. The DCF head [40, 45] is similar to the XCorr head, with two major differences. The first one is that it involves solving a ridge-regression problem to find the template $w = \omega(x)$ rather than using the original template x, so that the response map is given by

$$g(x, z) = \omega(x) \star z \tag{2}$$

More specifically, the DCF template $w = \omega(x)$ is a more discriminative template compared with the original template, and is obtained by solving

$$\arg\min_{w} \|w \star x - y\|^2 + \lambda \|w\|^2, \tag{3}$$

where y is an ideal response (here represented as a Gaussian function peaked at the center) and $\lambda \geq 0$ is the regularization coefficient typical of ridge regression. The solution to Eq. 3 can be computed efficiently in the Fourier domain [40, 45] as

$$\hat{w} = \frac{\hat{x} \odot \hat{y}^*}{\hat{x} \odot \hat{x}^* + \lambda} \tag{4}$$

where the hat notation $\hat{x} = \mathcal{F}(x)$ indicates the discrete Fourier Transform of x, y^* represents the complex conjugate of y and $\odot$ denotes the Hadamard (element-wise) product. The response map can be computed via inverse Fourier Transform $\mathcal{F}^{-1}$,

$$g(x, z) = \hat{w} \star z = \mathcal{F}^{-1}\left(\hat{w} \odot z\right) \tag{5}$$

Another difference *w.r.t* the XCorr head is that it is effective to update the template online by simple moving average [45], *i.e.* , $\hat{w}_t = \frac{\alpha \hat{x}_t \odot \hat{y}^* + (1-\alpha)\hat{x}_{t-1} \odot \hat{y}^*}{\alpha(\hat{x}_t \odot \hat{x}_t^* + \lambda) + (1-\alpha)(\hat{x}_{t-1} \odot \hat{x}_{t-1}^* + \lambda)}$. In contrast, with the XCorr head every frame is compared against the first one.

As shown in Table 2 and Table 3 from the main paper, for the tested architectures and appearance models we can see a clear advantage of DCF of XCorr (note that the difference was less significant in the original [40] paper, though the experiments were done with a shallower architecture).

Hyper-parameters. Following common practice [5, 23], we provide the Correlation Filter with a larger region of context in the template patch. To be specific, the template patch I_x is determined by expanding the height and width of the target bounding box by $k = 4.5$ times. The search patch is also determined by expanding the bounding box by same amount, and its center corresponds the latest estimated location of the target. To handle scale variation of the object, we consider $s = 3$ different search patches at different scales $0.985^{\{1,0,1\}}$. Template and search patches are cropped and resized to 520×520. This means that with a total stride of $r = 8$, we have feature maps of size 65×65. In the DCF head, we set the regularization coefficient to $\lambda = 1e^{-4}$, and the moving average momentum to $\alpha = 1e^{-2}$.

Box prop. hyper-parameters	Values
Template patch size	512×512
Search patch size	512×512
Box expanding coefficient	4.5
# Scales s	3
Scale factors	$1.0275^{\{-1,0,1\}}$
Scale penalties	$0.985^{\{1,0,1\}}$
Regularization coefficient λ	$1e^{-4}$
Moving average momentum α	$1e^{-2}$

B.2 Mask and Pose Propagation

In Section 2.3 we introduced the recursive mask propagation as $z_t = K_{t-1}^t z_{t-1}$. In practice, to provide more temporal context, we use a memory bank [21, 17] consisting of multiple former label maps as the source label z_m instead of a single label map z_{t-1}, *i.e.* $z_t = K_m^t z_m$. More specifically, the resulting source label map is obtained by concatenating all the label maps inside the memory bank, $z_m \in [0, 1]^{Ms}$, where s is the spatial size of a single label map and M is the size of the memory bank. The softmax computed for K_m^t is applied over all Ms points in the memory bank. The memory bank includes the first frame of the video, together with the latest $M - 1$ frames, and we choose $M = 6$. As suggested by MAST [21] and CRW [17], we also introduce the local attention technique, which restricts the source points considered for each target point to a local circle with radius $r = 12$. The hyper-parameter k for the k-NN used when computing the transition matrix K_m^t is set to $k = 10$.

Propagating pose key points is cast as propagating the mask of each individual key point, represented with the widely adopted Gaussian belief maps [48]. Each Gaussian has mean equal to the corresponding keypoint's location, and variance proportional to the subject's body size $\sigma = max(\eta s_{body}, 0.5)$. The body size is determined by,

$$s_{body} = \max(\max_p\{x_p\} - \min_p\{x_p\}, \max_p\{y_p\} - \min_p\{y_p\}) \tag{6}$$

where (x_p, y_p) are the coordinates of the p-th key point.

Mask/Pose prop. hyper-parameters	Values
Image size	Mask: 480×640 Pose: 320×320
Softmax temperature τ	0.05
Memory size M	6
Local attention radius r	12
k for k-nearest neighbor	10
Gaussian variance coefficient η	0.01

C *Association*

C.1 Association Algorithm

Motion cues: object states and Kalman Filtering. We employ a Kalman filter with constant velocity and linear motion model to handle motion cues in algorithms of the *association* type. We assume a generic setting where the camera is not calibrated and the ego-motion is not known. The object *states* are defined in an eight-dimensional space $(u, v, \gamma, h, \dot{u}, \dot{v}, \dot{\gamma}, \dot{h})$, where (u, v) indicate the position bounding box center, h the bounding-box height and $\gamma = \frac{h}{w}$ the aspect ratio. The latter four dimensions represent the respective velocities of the first four terms.

For the sake of simplicity we convert mask representations to bounding boxes. Let the coordinates of "in-mask" pixels form a set $\{(x_j, y_j)|j = 1, ...N\}$, where N is the number of mask pixels. Then, the center of the corresponding bounding box is obtained by averaging these coordinates, as $(u, v) = \frac{1}{N}\sum_{j=1}^{N}(x_j, y_j)$. We estimate the height of the bounding box as $h = \frac{2}{N}\sum_{j=1}^{N}\|y_j - h\|_1$. This estimation is analogous to the one suggested in the continuous case [25]. Consider a rectangle with scale $(2w, 2h)$ whose center locates at the origin of a 2D coordinate plane; by integrating over the points inside of the rectangle, we have $\frac{1}{h}\int_{-h}^{h}\|y\|_1 dy = \frac{2}{h}\int_0^h y dy = h$. For objects represented as a pose, we first convert pose keypoints to masks following Appendix C.2, and then convert masks to boxes.

For each timestep, the Kalman Filter [19] predicts current states of existing tracklets. If a new detection is associated to a tracklet, then the state of the detection is used to update the tracklet state. If a tracklet is not associated with any detection, its state is simply predicted without correction.

We use the (squared) Mahalanobis distance [49] to measure the "motion distance" between a newly arrived detection and an existing tracklet. Let us project the state distribution of the i-th tracklet into the measurement space and denote mean and covariance as $\boldsymbol{\mu}_i$ and $\boldsymbol{\Sigma}_i$, respectively. Then, the *motion distance* is given by

$$c^m_{i,j} = (\boldsymbol{o}_j - \boldsymbol{\mu}_i)^\top \boldsymbol{\Sigma}^{-1}(\boldsymbol{o}_j - \boldsymbol{\mu}_i) \tag{7}$$

where $\boldsymbol{o}_j$ indicates the observed (4D) state of the j-th detection. We observe that the Mahalanobis distance consistently outperforms Euclidean distance and IOU distance, likely thanks to the consideration of state estimation uncertainty. Using this metric also allows us to filter out unlikely matches by simply thresholding at 95% confidence interval [49]. We denote the filtering with an indicator function

$$b_{i,j} = \mathbb{1}[c^m_{i,j} > \eta]. \tag{8}$$

The threshold η can be computed from the inverse $\mathcal{X}^2$ distribution. In our case the degrees of freedom of the $\mathcal{X}^2$ distribution is 4, so the threshold $\eta = 9.4877$.

```
Algorithm 1: Hungarian Association
Input: Tracklet indices $\mathcal{T} = \{1, ..., N\}$, detection indices $\mathcal{D} = \{1, ..., M\}$. Hyperparameter $\lambda$.
Output: Set of matches $\mathcal{M}$, set of unmatched tracklets $\mathcal{T}_{remain}$, and detections $\mathcal{D}_{remain}$
Initialization: $\mathcal{M} \leftarrow \emptyset, \mathcal{D}_{remain} \leftarrow \mathcal{D}, \mathcal{T}_{remain} \leftarrow \mathcal{T}$ ;
for $t \in \mathcal{T}$ do
    Predict the state of the $t$-th tracklet using Kalman Filter
end
// main matching stage
Compute motion cost matrix $\boldsymbol{C}^m = [c^m_{i,j}]$ using Eq. 7;
Compute appearance cost matrix $\boldsymbol{C}^a = [c^a_{i,j}]$ using Eq. 9;
Compute final cost matrix $\boldsymbol{C} = \lambda\boldsymbol{C}^a + (1 - \lambda)\boldsymbol{C}^m$;
Compute gating matrix $\boldsymbol{B} = [b_{i,j}]$ using Eq. 8;
$[x_{i,j}]$ = Hungarian_assignment ($\boldsymbol{C}$);
$\mathcal{M} \leftarrow \mathcal{M} \cup \{(i, j)|b_{i,j} \cdot x_{i,j} > 0\}$ ;
$\mathcal{T}_{remain} \leftarrow \mathcal{T} \setminus \{i| \sum_j b_{i,j} \cdot x_{i,j} > 0\}$ ;
$\mathcal{D}_{remain} \leftarrow \mathcal{D} \setminus \{j| \sum_i b_{i,j} \cdot x_{i,j} > 0\}$ ;
// second matching stage
Compute IOU cost matrix $\boldsymbol{C}^g$ between $\mathcal{T}_{remain}$ and $\mathcal{D}_{remain}$.;
$[x_{i,j}]$ = Hungarian_assignment ($\boldsymbol{C}$);
$\mathcal{M} \leftarrow \mathcal{M} \cup \{(i, j)|x_{i,j} > 0\}$ ;
$\mathcal{T}_{remain} \leftarrow \mathcal{T}_{remain} \setminus \{i| \sum_j x_{i,j} > 0\}$ ;
$\mathcal{D}_{remain} \leftarrow \mathcal{D}_{remain} \setminus \{j| \sum_i x_{i,j} > 0\}$ ;
```

Association algorithm. Algorithm 1 outlines the association procedure for a *single timestamp*. The algorithm takes as input a set of tracklets $\mathcal{T} = \{1, ..., N\}$ and detections $\mathcal{D} = \{1, ..., M\}$. First, we predict the current states of the all tracklets using the Kalman Filter. Then we perform the main matching stage. In this stage, we compute a motion cost matrix $\boldsymbol{C}^m$ using Eq 7, and compute an appearance cost matrix $\boldsymbol{C}^a$ using the RSM metric described in Section 2.4,

$$c^a_{i,j} = \texttt{RSM}(i, j) \tag{9}$$

The final cost matrix is the linear combination of the two cost matrices $\boldsymbol{C} = \lambda\boldsymbol{C}^a + (1 - \lambda)\boldsymbol{C}^m$. We set $\lambda = 0.99$. A Hungarian solver takes the cost matrix $\boldsymbol{C}$ as input and outputs matches $[x_{i,j}]$. We then filter out unrealistic matches using Eq 8. For the remaining tracklets and detections which failed matching, we perform a second matching stage using IOU distance as the cost matrix. Remaining tracklets and detections are output by the association algorithm, further steps (described below) determine if a remaining tracklet should be terminated or if a new identity should be initialized from a remaining detection.

Tracklet termination and initialization. If a tracklet fails to be matched with a newly arrived detection with Algorithm 1, we mark it as inactive. To account for short occlusions, inactive tracklets can still be restored if they are found to be matching with a new detection. We record a "lost age" for each inactive tracklet. If the lost age is greater than a pre-given time, the tracklet would be removed from the current tracklet pool. The lost age is set to 1 second in our experiments.

If a detection fails to match existing tracklets with Algorithm 1, it could correspond to a new tracklet. However, this would result in the creation of frequent brief "spurious" tracklets, containing one detection only. To cope with this issue, similarly to [49] we only initialize a new tracklet if a new detection appears in two consecutive frames (and the IOU between consecutive boxes is at least 0.8).

C.2 Pose-to-Mask Conversion

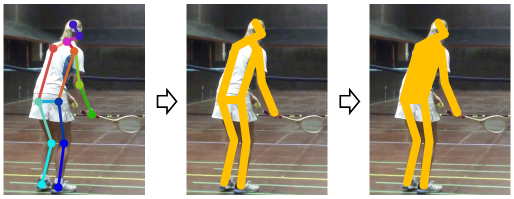

Given the key points' location of a target person, we convert the pose into a binary mask in two steps. First, the key points are connected to form a skeleton, where the width of each segment forming this skeleton is proportional to the body size with a linear coefficient $\eta_p = 0.05$, and the

Detector	DPM			FRCNN			SDP			FairMOT-Det			w/ motion
Metrics	IDF1	IDs	MOTA	IDF1	IDs	MOTA	IDF1	IDs	MOTA	IDF1	IDs	MOTA	
CF	36.5	748	29.8	51.3	480	**50.2**	60.9	848	64.5	75.5	550	**82.9**	✓
GPF	34.4	1261	29.3	50.0	530	**50.2**	60.8	985	**64.8**	76.4	534	**82.9**	✓
GF	36.3	674	29.8	52.2	479	**50.2**	62.0	**759**	64.6	75.9	**499**	**82.9**	✓
ReID	**40.0**	619	29.8	54.9	461	50.1	**67.1**	811	64.5	78.4	545	82.8	✓
RSM	39.6	**513**	**30.0**	**55.6**	**431**	**50.2**	64.2	762	64.5	**78.6**	543	82.7	✓
CF	26.3	1381	22.8	40.4	820	47.4	46.7	1525	58.2	60.4	1599	76.6	
GPF	29.5	782	25.5	43.7	517	48.2	48.8	1337	59.5	57.2	1414	77.4	
GF	24.9	1298	22.4	41.7	526	48.1	51.0	**960**	60.6	65.3	868	78.9	
ReID	**33.1**	**637**	**25.9**	47.0	692	47.5	53.3	1250	58.5	64.8	1448	75.9	
RSM	28.1	805	25.4	**51.5**	**414**	**49.8**	**58.6**	999	**62.7**	**74.5**	**605**	**82.3**	

Table 1: Comparison between different similarity metrics for association, tested on MOT-16 *train* split. We provide results that (1) use motion cues and (2) discard motion cues. The best results are **bolded** and the second best results are underlined.

Methods	IDF1	IDs	MOTA
CF	38.6	6384	**41.8**
GPF	38.3	6245	**41.8**
GF	39.3	5858	**41.8**
ReID	39.1	6442	41.7
RSM	**41.3**	**5552**	41.6

Table 2: Comparison between different similarity metrics for association, tested on MOT-20 [9] with the provided detector.

Methods	IDF1	IDs	sMOTSA
CF	62.8	1529	80.7
GPF	60.7	1071	82.4
RSM	**66.5**	**808**	**83.4**

Table 3: Comparison between different similarity metrics for *association*, tested on MOTS [43] *train* split based on the segmentation masks provided by the COSTA$_{st}$ [1] tracker.

body size is computed with Eq. 6. Second, we fill closed polygons inside the pose skeleton, since the parts inside the polygon usually belong to the target object.

D Ablations for the Reconstruction Similarity Metric (RSM)

In Section 2.4 we claimed that the good tracking performance of UniTrack on association-type tasks is largely attributed to the proposed Reconstruction Similarity Metric (RSM). In this section, we provide results of several baseline methods in order to validate the effectiveness of RSM. These baseline are described below.

Center feature (CF). For a given observation feature $d_j \in \mathbb{R}^{s_{d_j} \times C}$ of a bounding box or a mask, we compute the location of its center of mass and extract the corresponding point feature (a single C-dim vector) as representation of this observation. Cosine similarity is computed to measure how likely two observations belong to the same identity. Using center feature to represent an object is a straightforward strategy, widely used in tracking tasks [58, 47, 55]. The benefit of CF is that it can handle objects in any observation format, *e.g.* boxes or masks, while the drawback is also obvious: it is a local feature and cannot represent the complete information of the object.

Global feature (GF). For a given observation feature $d_j \in \mathbb{R}^{s_{d_j} \times C}$, we concatenate the s_{d_j} point features and obtain a single global feature vector with length $s_{d_j}C$. Cosine similarity is computed to measure how likely two observations belong to the same identity. Note that only representations with fixed s_{d_j} are feasible in this case. For this reason, we only provide results for GF on the MOT task, where observations are bounding boxes that can be resized to a fixed size. The benefit of GF is that it preserve complete information of the observation, while the main drawback is that local features may not align between a pair of samples. Therefore, global feature is only applicable in cases where samples are aligned with pre-processing, *e.g.* in face recognition [13]

Global-pooled feature (GPF). Similar to the global feature, but averaging is performed along the s_{d_j} dimension to obtain a single feature vector with length C. Cosine similarity then is computed to measure how likely it is that the two observations belong to the same identity. A large body of re-identification (ReID) approaches [38, 59, 37] employ global-pooled feature (on fully supervised learned feature maps). The benefit and drawback are similar to center feature.

Methods	PCK@0.1	PCK@0.2
TimeCycle [46]	57.3	78.1
UVC [25]	58.6	79.6
CRW [17]	**59.0**	**83.2**
I18 (reported in [17])	53.8	74.6
I18 (UniTrack)	58.3	80.5
Yang et al. [53]	**68.7**	**92.1**

Table 4: Results of pose propagation on JH-MDB [18] dataset. I18 refers to using ImageNet pre-trained ResNet-18 as the appearance model.

Methods	mAP↑
FEELVOS [42]	26.9
SipMask [6]	**32.5**
OSMN† [54]	27.5
DeepSORT† [49]	26.1
MTRCNN† [52]	30.3
UniTrack†	30.1

Table 5: VIS results@YoutubeVIS [52] *val* split. † indicates methods using the same observations (segmentation masks in every single frames).

Supervised ReID feature (ReID). For a given image cropped from a bounding box, we employ an strong, off-the-shelf person ReID model to extract a single feature vector with length C, and compute cosine similarity between observations. The model uses a ResNet-50 [15] architecture and is trained with the joint set of three widely-used datasets: Market-1501 [56], CUHK-03 [24], and DukeMTMC-ReID [34]. Using supervised ReID models to extract appearance features is widely used in existing multi-object tracking approaches [39, 27, 35]. Considering large amount of identity labels are leveraged in training, supervised ReID models usually show good association accuracy.

Note that for CF, GF, GPF, and the proposed RSM, we employ the same appearance model (ImageNet pre-trained ResNet-18) for fair comparison. For a broad comparison, we provide results obtained with different detectors and on different datasets. We adopt the following detectors and test on MOT-16 [29] *train* split (listed with detection accuracy from low to high): DPM [14], Faster R-CNN [33] (FRCNN), SDP [51], and FairMOT [55].

Results are shown in Table 1. We first apply the full association algorithm, *i.e.* using both appearance and motion cues. In this case (first half of the table), RSM consistently outperforms CF, GF, GPF baselines, and even surpasses the supervised ReID features in several cases, *e.g.* with FRCNN and FairMOT detectors. In the second half of the table, we show results in which only appearance cues are used, so that the difference between metrics (which are based on appearance) can be better emphasized. In this case, the gaps between different methods are more significant than in the previous case, and RSM still consistently outperforms CF, GF, and GPF. Furthermore, RSM also surpasses the strong supervised ReID feature with all detectors, except for DPM. This suggests that RSM can be an effective similarity metric for tasks that have *association* at their core.

To show the generality of the results, we also experiment on different datasets and different tasks. Table 2 shows comparisons on the MOT-20 [9] *train* split for the MOT task (box observations). The MOT-20 dataset is specialized for the extreme crowded person tracking scenario. Table 3 presents results on MOTS [43] *train* split for the MOTS task (mask observations). Note for the MOTS task, since the observations (masks) vary in size, it is not feasible to apply the GF strategy. Results show that the proposed RSM yields significantly higher IDF1 scores on both datasets.

E More Tracking Tasks

In this section we present two more tasks that UniTrack can address.

The first task is human **Pose Propagation** on the JHMDB [18] dataset: each video contains a *single* person of interest, and the pose keypoints are provided in the first frame of the video only. The goal here is to predict the pose of the person throughout the video. Note that this is different from the previously mentioned PoseTrack task: PoseTrack mainly focuses on association between different identities, while in Pose Propagation we aim at propagating the pose of a single identity.

Results are shown in Table 4. We report a higher result with ImageNet pre-trained ResNet-18 compared with in previous work [17, 25] (58.3 *v.s.* 53.8 PCK@0.1). With this result, we observe the best self-supervised method CRW [17] does not beat the ImageNet pre-trained representation by a significant margin (only +0.7 PCK@1). This again validates our second finding in Section 3.2: a vanilla ImageNet-trained representation is surprisingly effective.

Method	TS sup.	TrackingNet [31]		TC-128 [26]		TLP [30]		LaSOT [12]		OxUvA [41]
		Succ.	Prec.	Succ.	Prec.	Succ.	Prec.	Succ.	Prec.	MaxGM
KCF [16]	N	41.9	44.7	38.7	54.9	8.4	6.3	17.8	-	-
ECO [7]	N	56.1	48.9	-	-	20.2	21.2	32.4	30.1	0.314
Staple [4]	N	-	-	-	-	-	-	-	-	0.261
BACF [20]	N	-	-	-	-	-	-	-	-	0.281
SiamFC [5]	Y	57.1	66.3	50.3	68.8	23.5	28.4	33.6	33.9	0.313
CFNet [40]	Y	53.3	57.8	-	-	-	-	27.5	-	-
SiamRPN [23]	Y	-	-	-	-	-	-	-	-	-
SiamRPN++ [22]	Y	73.3	69.4	-	-	-	-	49.6	49.1	-
LUDT [44]	N	46.9	54.3	51.5	67.1	-	-	26.2	-	-
LUDT+ [44]	N	49.5	56.3	55.2	72.5	-	-	30.5	-	-
UnTrack	N	59.1	51.2	54.5	73.1	25.4	23.2	35.1	32.6	0.334

Table 6: Results on more SOT datasets. An ImageNet pre-trained representation with a ResNet-50 architecture is employed as the appearance model within UniTrack. "TS sup." indicates whether the method requires task-specific supervision.

The second task is **Video Instance Segmentation (VIS)**. The problem of VIS is similar to Multiple Object Tracking and Segmentation (MOTS), but its setup differs in the following aspects: first, the object categories are fairly diverse (40 different categories), while in MOTS objects are mostly persons and vehicles. This also requires the trackers tackling the VIS task to handle objects from different classes within the same scene. Second, the evaluation metrics are different. In MOTS, the MOT-like metrics (CLEAR [3], IDF-1/IDs, and HOTA [28]) are used, which implicitly encourages methods to focus on outputting temporally consistent trajectories. Instead, for VIS the evaluation metric is spatial-temporal mAP, a temporal extension of the vanilla mAP which is usually used in detection and segmentation tasks. The mAP metric significantly biases towards segmentation and classification accuracy in single frames, thus being less informative for evaluating "tracking" accuracy.

Results on VIS task are shown in Table 5. We adopt an identical segmentation model to the one of MaskTrackRCNN [52], and observe only a 0.2 difference in mAP. For further comparison, we also provide results of two other association methods, OSMN [54] and DeepSORT [49], providing them with the same observations as used by UniTrack. Note how UniTrack boasts better accuracy than both methods (30.0 *v.s.* 27.5 and 26.1 mAP). Comparing with an state-of-the-art model, SipMask [6], our result is also comparable with -2.4 point mAP. We believe if equipped with more advanced single frame segmentation model, the mAP would be further improved.

F SOT results on more datasets

To further validate the general validity of our experiments, we provide more results for the SOT task by testing on more recent datasets that contain large-scale and long-term videos.

The results in Table 6 show a very similar trend to the one already observed for OTB (Table 3e in the main text): For the SOT task, UniTrack with ImageNet features has comparable performance to the one of the recent LUDT+, which like UniTrack does not require task-specific supervision, but can only be used for SOT. Again, similarly to what was reported for OTB, UniTrack is outperformed by recent methods such as SiamRPN++. This is to be expected, as SiamRPN++ is specifically designed for SOT and trained in a supervised fashion on several large-scale video datasets.

G Additional Correlation Studies

In Section 3.3 (main paper) we investigated the correlation between tracking performance and ImageNet "linear probe" accuracy for different SSL models. In this section, we provide more results and discussions by studying the correlation between tracking performance and several other downstream tasks when using the appearance model from the many SSL methods under consideration. For non-tracking tasks, we report numbers from [10] and plot them against tracking performance in Figure 1.

We report three tasks: surface normal estimation on the NYUv2 [36] dataset, where the mean angular error is used as the evaluation metric (the lower the better); Object detection on Pascal VOC [11],

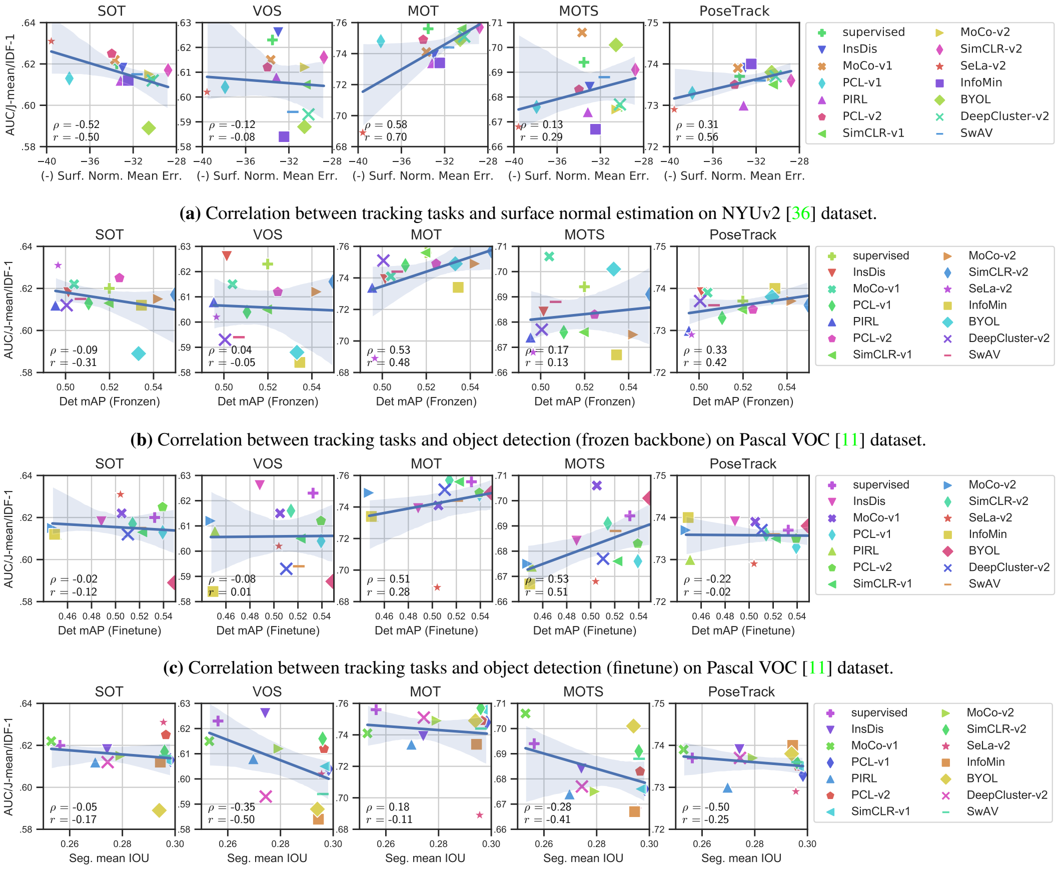

(a) Correlation between tracking tasks and surface normal estimation on NYUv2 [36] dataset.

(b) Correlation between tracking tasks and object detection (frozen backbone) on Pascal VOC [11] dataset.

(c) Correlation between tracking tasks and object detection (finetune) on Pascal VOC [11] dataset.

(d) Correlation between tracking tasks and semantic segmentation on ADE20k [57] dataset.

Figure 1: Correlation study between tracking tasks and other tasks for SSL models. On the y-axes we plot tracking performance, and on x-axes performance of the other tasks. Spearman's r and Pearson's ρ are shown in the left bottom corner of each plot, indicating how the two axes are correlated.

with performance measured in mAP (the higher the better); Semantic segmentation on ADE20k [57] dataset, with performance measured in mean IOU (the higher the better). In each subfigure, we plot the performance of five tracking tasks along the y-axes, and performance of the other task along the x-axes. Note that we actually use *negative* mean error for surface normal estimation, to represent *accuracy*. As in the main paper, we compute two types of correlation coefficient: Spearman' r and Pearson's ρ, and report them in the left bottom corner of each plot. Several interesting findings can be observed:

(a) Correlation between tracking and surface normal prediction performance is fairly strong. Results are shown in Figure 1a. For instance, $r = 0.70$ for surface normal error *v.s.* MOT accuracy, and 0.56 for surface normal error *v.s.* PoseTrack accuracy. Interestingly, the behavior of SOT is in contrast with MOT and PoseTrack: SOT accuracy is moderately negative correlated ($r = -0.50$) with surface normal estimation accuracy. VOS presents a similar trend to the one of SOT, but with a lower correlation coefficient.

(b) Object detection is moderately correlated with association-type tracking tasks. For object detection, we consider two setups: one is to freeze the representation and only train the additional classification/regression head; the other is to finetune the whole network in an end-to-end manner. Results are shown in Figure 1b and 1c respectively. In general, MOT and PoseTrack are moderately correlated with object detection under the frozen setting ($r = 0.48$ for MOT and and $r = 0.42$ for PoseTrack), and MOTS is moderately correlated with object detection under the finetune setting ($r = 0.51$). Propagation-type tasks are poorly correlated with object detection results under both settings ($|\rho| < 0.10$). We speculate that, in this case, positive correlation might be due to the fact that

both object detection and association-type tracking require discriminative features at the level of the object.

(c) Semantic segmentation is slightly negative correlated with tracking tasks. As can be observed in Figure 1d, correlation coefficients between segmentation accuracy and tracking performance are mildly negative. Among these results, VOS is the task that is most (negatively) correlated with segmentation, with $r = -0.50$. MOTS and PoseTrack are also mildly correlated, with $r = -0.41$ and $r = -0.25$ respectively. We speculate that negative correlation might be cause to the fact that tracking and segmentation require features with contradictory properties. Consider two different instances that belongs to the same category, *i.e.* two different pedestrian. For segmentation, the task requires pixel-wise classification, meaning that pixels inside the two instances should be equally classified into the same "pedestrian" class, thus their features should be *similar* (close to the class center). In contrast, for tracking tasks, it is required to distinguish different instances from the same class, otherwise a tracker would easily fail when objects overlap with each other. Therefore, point features inside the two different pedestrian are expected to be *dissimilar*.

References

[1] Costa_st tracker. https://motchallenge.net/method/MOTS=87&chl=17.

[2] Mykhaylo Andriluka, Umar Iqbal, Eldar Insafutdinov, Leonid Pishchulin, Anton Milan, Juergen Gall, and Bernt Schiele. Posetrack: A benchmark for human pose estimation and tracking. In *CVPR*, 2018.

[3] Keni Bernardin and Rainer Stiefelhagen. Evaluating multiple object tracking performance: the clear mot metrics. *EURASIP Journal on Image and Video Processing*, 2008:1–10, 2008.

[4] Luca Bertinetto, Jack Valmadre, Stuart Golodetz, Ondrej Miksik, and Philip HS Torr. Staple: Complementary learners for real-time tracking. In *CVPR*, 2016.

[5] Luca Bertinetto, Jack Valmadre, Joao F Henriques, Andrea Vedaldi, and Philip HS Torr. Fully-convolutional siamese networks for object tracking. In *ECCV workshops*, 2016.

[6] Jiale Cao, Rao Muhammad Anwer, Hisham Cholakkal, Fahad Shahbaz Khan, Yanwei Pang, and Ling Shao. Sipmask: Spatial information preservation for fast image and video instance segmentation. *ECCV*, 2020.

[7] Martin Danelljan, Goutam Bhat, Fahad Shahbaz Khan, and Michael Felsberg. Eco: Efficient convolution operators for tracking. In *CVPR*, 2017.

[8] Patrick Dendorfer, Aljosa Osep, Anton Milan, Konrad Schindler, Daniel Cremers, Ian Reid, Stefan Roth, and Laura Leal-Taixé. Motchallenge: A benchmark for single-camera multiple target tracking. *International Journal of Computer Vision*, 129(4):845–881, 2021.

[9] Patrick Dendorfer, Hamid Rezatofighi, Anton Milan, Javen Shi, Daniel Cremers, Ian Reid, Stefan Roth, Konrad Schindler, and Laura Leal-Taixé. Mot20: A benchmark for multi object tracking in crowded scenes. *arXiv:2003.09003*, 2020.

[10] Linus Ericsson, Henry Gouk, and Timothy M Hospedales. How well do self-supervised models transfer? In *CVPR*, 2021.

[11] Mark Everingham, Luc Van Gool, Christopher KI Williams, John Winn, and Andrew Zisserman. The pascal visual object classes (voc) challenge. *International journal of computer vision*, 88(2):303–338, 2010.

[12] Heng Fan, Liting Lin, Fan Yang, Peng Chu, Ge Deng, Sijia Yu, Hexin Bai, Yong Xu, Chunyuan Liao, and Haibin Ling. Lasot: A high-quality benchmark for large-scale single object tracking. In *CVPR*, 2019.

[13] Masoud Faraki, Xiang Yu, Yi-Hsuan Tsai, Yumin Suh, and Manmohan Chandraker. Cross-domain similarity learning for face recognition in unseen domains. *arXiv:2103.07503*, 2021.

[14] Pedro F Felzenszwalb, Ross B Girshick, and David McAllester. Cascade object detection with deformable part models. In *CVPR*, 2010.

[15] Kaiming He, Xiangyu Zhang, Shaoqing Ren, and Jian Sun. Deep residual learning for image recognition. In *CVPR*, 2016.

[16] João F Henriques, Rui Caseiro, Pedro Martins, and Jorge Batista. High-speed tracking with kernelized correlation filters. *IEEE TPAMI*, 2014.

[17] Allan Jabri, Andrew Owens, and Alexei A Efros. Space-time correspondence as a contrastive random walk. In *NeurIPS*, 2020.

[18] H. Jhuang, J. Gall, S. Zuffi, C. Schmid, and M. J. Black. Towards understanding action recognition. In *ICCV*, 2013.

[19] Rudolph Emil Kalman. A new approach to linear filtering and prediction problems. 1960.

[20] Hamed Kiani Galoogahi, Ashton Fagg, and Simon Lucey. Learning background-aware correlation filters for visual tracking. In *ICCV*, 2017.

[21] Zihang Lai, Erika Lu, and Weidi Xie. Mast: A memory-augmented self-supervised tracker. In *CVPR*, 2020.

[22] Bo Li, Wei Wu, Qiang Wang, Fangyi Zhang, Junliang Xing, and Junjie Yan. Siamrpn++: Evolution of siamese visual tracking with very deep networks. In *CVPR*, 2019.

[23] Bo Li, Junjie Yan, Wei Wu, Zheng Zhu, and Xiaolin Hu. High performance visual tracking with siamese region proposal network. In *CVPR*, 2018.

[24] Wei Li, Rui Zhao, Tong Xiao, and Xiaogang Wang. Deepreid: Deep filter pairing neural network for person re-identification. In *CVPR*, 2014.

[25] Xueting Li, Sifei Liu, Shalini De Mello, Xiaolong Wang, Jan Kautz, and Ming-Hsuan Yang. Joint-task self-supervised learning for temporal correspondence. In *NeurIPS*, 2019.

[26] Pengpeng Liang, Erik Blasch, and Haibin Ling. Encoding color information for visual tracking: Algorithms and benchmark. *IEEE TIP*, 2015.

[27] Chen Long, Ai Haizhou, Zhuang Zijie, and Shang Chong. Real-time multiple people tracking with deeply learned candidate selection and person re-identification. In *ICME*, 2018.

[28] Jonathon Luiten, Aljosa Osep, Patrick Dendorfer, Philip Torr, Andreas Geiger, Laura Leal-Taixé, and Bastian Leibe. Hota: A higher order metric for evaluating multi-object tracking. *IJCV*, 2020.

[29] Anton Milan, Laura Leal-Taixé, Ian Reid, Stefan Roth, and Konrad Schindler. Mot16: A benchmark for multi-object tracking. *arXiv:1603.00831*, 2016.

[30] Abhinav Moudgil and Vineet Gandhi. Long-term visual object tracking benchmark. In *ACCV*, 2018.

[31] Matthias Muller, Adel Bibi, Silvio Giancola, Salman Alsubaihi, and Bernard Ghanem. Trackingnet: A large-scale dataset and benchmark for object tracking in the wild. In *ECCV*, 2018.

[32] F. Perazzi, J. Pont-Tuset, B. McWilliams, L. Van Gool, M. Gross, and A. Sorkine-Hornung. A benchmark dataset and evaluation methodology for video object segmentation. In *CVPR*, 2016.

[33] Shaoqing Ren, Kaiming He, Ross Girshick, and Jian Sun. Faster r-cnn: Towards real-time object detection with region proposal networks. In *ICCV*, 2015.

[34] Ergys Ristani, Francesco Solera, Roger Zou, Rita Cucchiara, and Carlo Tomasi. Performance measures and a data set for multi-target, multi-camera tracking. In *ECCV*, 2016.

[35] Ergys Ristani and Carlo Tomasi. Features for multi-target multi-camera tracking and re-identification. In *CVPR*, 2018.

[36] Nathan Silberman, Derek Hoiem, Pushmeet Kohli, and Rob Fergus. Indoor segmentation and support inference from rgbd images. In *ECCV*, 2012.

[37] Yifan Sun, Qin Xu, Yali Li, Chi Zhang, Yikang Li, Shengjin Wang, and Jian Sun. Perceive where to focus: Learning visibility-aware part-level features for partial person re-identification. In *CVPR*, 2019.

[38] Yifan Sun, Liang Zheng, Yi Yang, Qi Tian, and Shengjin Wang. Beyond part models: Person retrieval with refined part pooling (and a strong convolutional baseline). In *ECCV*, 2018.

[39] Siyu Tang, Mykhaylo Andriluka, Bjoern Andres, and Bernt Schiele. Multiple people tracking by lifted multicut and person re-identification. In *CVPR*, 2017.

[40] Jack Valmadre, Luca Bertinetto, Joao Henriques, Andrea Vedaldi, and Philip HS Torr. End-to-end representation learning for correlation filter based tracking. In *CVPR*, 2017.

[41] Jack Valmadre, Luca Bertinetto, Joao F Henriques, Ran Tao, Andrea Vedaldi, Arnold WM Smeulders, Philip HS Torr, and Efstratios Gavves. Long-term tracking in the wild: A benchmark. In *ECCV*, 2018.

[42] Paul Voigtlaender, Yuning Chai, Florian Schroff, Hartwig Adam, Bastian Leibe, and Liang-Chieh Chen. Feelvos: Fast end-to-end embedding learning for video object segmentation. In *CVPR*, 2019.

[43] Paul Voigtlaender, Michael Krause, Aljosa Osep, Jonathon Luiten, Berin Balachandar Gnana Sekar, Andreas Geiger, and Bastian Leibe. Mots: Multi-object tracking and segmentation. In *CVPR*, 2019.

[44] Ning Wang, Wengang Zhou, Yibing Song, Chao Ma, Wei Liu, and Houqiang Li. Unsupervised deep representation learning for real-time tracking. *IJCV*, 2020.

[45] Qiang Wang, Jin Gao, Junliang Xing, Mengdan Zhang, and Weiming Hu. Dcfnet: Discriminant correlation filters network for visual tracking. *arXiv:1704.04057*, 2017.

[46] Xiaolong Wang, Allan Jabri, and Alexei A Efros. Learning correspondence from the cycle-consistency of time. In *CVPR*, 2019.

[47] Zhongdao Wang, Liang Zheng, Yixuan Liu, and Shengjin Wang. Towards real-time multi-object tracking. In *ECCV*, 2020.

[48] Shih-En Wei, Varun Ramakrishna, Takeo Kanade, and Yaser Sheikh. Convolutional pose machines. In *CVPR*, 2016.

[49] Nicolai Wojke, Alex Bewley, and Dietrich Paulus. Simple online and realtime tracking with a deep association metric. In *ICIP*, 2017.

[50] Yi Wu, Jongwoo Lim, and Ming-Hsuan Yang. Online object tracking: A benchmark. In *CVPR*, 2013.

[51] Fan Yang, Wongun Choi, and Yuanqing Lin. Exploit all the layers: Fast and accurate cnn object detector with scale dependent pooling and cascaded rejection classifiers. In *CVPR*, 2016.

[52] Linjie Yang, Yuchen Fan, and Ning Xu. Video instance segmentation. In *ICCV*, 2019.

[53] Linjie Yang, Yanran Wang, Xuehan Xiong, Jianchao Yang, and Aggelos K Katsaggelos. Efficient video object segmentation via network modulation. In *CVPR*, 2018.

[54] Linjie Yang, Yanran Wang, Xuehan Xiong, Jianchao Yang, and Aggelos K Katsaggelos. Efficient video object segmentation via network modulation. In *CVPR*, 2018.

[55] Yifu Zhang, Chunyu Wang, Xinggang Wang, Wenjun Zeng, and Wenyu Liu. Fairmot: On the fairness of detection and re-identification in multiple object tracking. *arXiv:2004.01888*, 2020.

[56] Liang Zheng, Liyue Shen, Lu Tian, Shengjin Wang, Jingdong Wang, and Qi Tian. Scalable person re-identification: A benchmark. In *ICCV*, 2015.

[57] Bolei Zhou, Hang Zhao, Xavier Puig, Sanja Fidler, Adela Barriuso, and Antonio Torralba. Scene parsing through ade20k dataset. In *CVPR*, 2017.

[58] Xingyi Zhou, Vladlen Koltun, and Philipp Krähenbühl. Tracking objects as points. In *ECCV*, 2020.

[59] Kuan Zhu, Haiyun Guo, Zhiwei Liu, Ming Tang, and Jinqiao Wang. Identity-guided human semantic parsing for person re-identification. In *ECCV*, 2020.